AIAA JOURNAL
Vol. 40, No. 5, May 2002

High-Order Semi-Implicit Schemes for Unsteady Compressible Flow Simulations

Haibo Dong* and Xiaolin Zhong†
University of California, Los Angeles, Los Angeles, California 90095

Direct numerical simulation of stability and transition of compressible boundary layers requires high-order-accurate and computationally efficient numerical methods to resolve a wide range of time- and length scales associated with wave fields in the boundary layers. Explicit methods have been used mainly in such simulations to advance the compressible Navier–Stokes equations in time. However, the small wall-normal grid sizes for viscous flow simulations impose a severe stability restriction on the allowable time steps in simulations using the explicit method. This requires implicit treatment to our numerical method. Although fully implicit methods are often used in steady-flow calculations to remove the stability restriction on time steps, they are seldom used in transient flow simulations because the time steps used in time-accurate calculations are often not large enough to offset high computational cost of using fully implicit methods. A high-order-accurate semi-implicit scheme is presented for the direct numerical simulation of the stability and transition of compressible wall-bounded flows. The efficiency and accuracy of the semi-implicit scheme are evaluated by applying the method to transient flow simulations of several supersonic and hypersonic wall-bounded flow stability problems.

Introduction

THE numerical methods presented in this paper are motivated by our research of direct numerical simulation of stability and transition of compressible boundary layer. In recent years direct numerical simulation (DNS) has become a powerful tool in the study of fundamental flow physics of the stability and transition of compressible boundary layers.[1–6] In such requiring high order both in space and in time-accurate simulations, the unsteady Navier–Stokes equations are computed, without using any empirical model, to resolve all time- and length scales associated with wave fields in the boundary layers.

The DNS studies of the stability and transition of compressible boundary layers over flat plates have been carried out by many researchers using various methods. Kleiser and Zang[1] had reviewed the status of numerical simulations and methods for the DNS of compressible boundary layers and used compact scheme in spatial discretization. Erlebacher and Hussaini[2] used the explicit Fourier–Chebyshev collocation method to do numerical experiments in supersonic boundary-layer stability. Fasel et al.[3] implemented the explicit fourth-order finite difference method in DNS of oblique breakdown transition in supersonic boundary layers. Eibler and Bestek[4] used a modified explicit MacCormack predictor-corrector scheme of second-order accuracy in time and fourth-order spatial discretization to do spatial numerical simulations of nonlinear transition phenomena in supersonic boundary layers. Adams[5] did numerical simulation of transition in a compressible flat-plate boundary layer by using an explicit spectral/finite difference scheme. In Guo et al.'s[6] numerical simulations of supersonic boundary-layer transition, the explicit Runge–Kutta scheme in time and the high-order compact scheme in space were used. Generally, in these simulations high-order finite difference methods or spectral methods are used to discretize the governing conservation equations in space. The resulting semi-discrete systems of equations are then advanced in time using explicit time-stepping schemes, such as the third-order Runge–Kutta schemes.

Although most of the previous DNS work for compressible flow used explicit methods, simulations using explicit schemes for viscous flow simulation are not computationally efficient because the grid sizes in the wall-normal direction are much smaller than those in the streamwise direction for viscous flow simulations. The small wall-normal grid sizes impose severe stability restriction on the allowable time steps in simulations using explicit schemes, where the time steps required by the stability requirement in the calculations are much smaller than those needed by accuracy consideration so that it is difficult to perform the simulation in reasonable computation time. As a result, DNS of compressible boundary layers are an order of magnitude more computationally expensive than their incompressible simulations. The removal of the restriction on the time steps for explicit schemes requires implicit treatment in numerical computations. However, fully implicit methods, which advance all derivatives in time using implicit time-stepping schemes, are seldom used for transient flows because the time steps used in unsteady flow calculations are often not large enough to offset high computational cost of using implicit methods because of the accuracy requirement in computing the development of transient instability waves in the streamwise direction. Therefore, the appropriate method that can meet the requirement for both computational efficiency and numerical accuracy in the DNS studies is the semi-implicit method, which only treats the derivatives in the wall-normal direction implicitly. The idea of the semi-implicit method is not new; it has been a common method for DNS of incompressible turbulence, which typically treated viscous parts of the equations implicitly, or simulations of chemical reaction, which treated the stiff term implicitly and used second-order fractional step in time discretization.

This paper presents a high-order semi-implicit scheme for the DNS of the stability and transition of compressible wall-bounded flows. The unsteady compressible Navier–Stokes equations are discretized in space using high-order finite difference schemes. The spatial discretization terms of the governing equations are separated into stiff terms, involving derivatives along the wall-normal direction only, and nonstiff terms for the rest of the equations. The split equations are advanced in time using semi-implicit temporal schemes, which lead to efficient computations of block seven-diagonal systems of implicit equations. In this paper a set of second- and third-order semi-implicit Runge–Kutta schemes[7] are used for the robust and accurate temporal discretization of stiff equations for the DNS of unsteady compressible flows. For the direct numerical simulation of hypersonic boundary layers behind bow shocks over blunt bodies, a high-order shock-fitting numerical scheme developed by Zhong[8] is used to treat the presence of shock waves. The efficiency and temporal accuracy of the semi-implicit scheme are

Received 22 November 2000; revision received 1 November 2001; accepted for publication 20 November 2001.

*Ph.D. Student, Mechanical and Aerospace Engineering Department; haibo@seas.ucla.edu. Student Member AIAA.

†Associate Professor, Mechanical and Aerospace Engineering Department; xiaolin@seas.ucla.edu. Associate Fellow AIAA.

evaluated by applying the method to several transient flow simulations of compressible boundary-layer stability.

Governing Equations

The governing equations are the unsteady three-dimensional Navier–Stokes equations written in a conservation-law form:

$$\frac{\partial U}{\partial t}+\frac{\partial F_j}{\partial x_j}+\frac{\partial F_{vj}}{\partial x_j}=0 \tag{1}$$

where

$$U=\{\rho,\ \rho u_1,\ \rho u_2,\ \rho u_3,\ e\} \tag{2}$$

$$F_j=\begin{Bmatrix}\rho u_j\\ \rho u_1u_j+p\delta_{1j}\\ \rho u_2u_j+p\delta_{2j}\\ \rho u_3u_j+p\delta_{3j}\\ (e+p)\,u_j\end{Bmatrix},\qquad F_{vj}=\begin{Bmatrix}0\\ \tau_{1j}\\ \tau_{2j}\\ \tau_{3j}\\ \tau_{jk}u_k-q_j\end{Bmatrix} \tag{3}$$

$$p=\rho RT \tag{4}$$

$$e=\rho\left(c_vT+\frac{\rho}{2}u_ku_k\right) \tag{5}$$

$$\tau_{ij}=-\mu\left(\frac{\partial u_i}{\partial x_j}+\frac{\partial u_j}{\partial x_i}\right)+\frac{2\mu}{3}\frac{\partial u_k}{\partial x_k}\delta_{ij} \tag{6}$$

$$q_j=-\kappa\frac{\partial T}{\partial x_j} \tag{7}$$

The details for the expressions just listed can be found in Ref. 8. The viscosity and heat conductivity coefficients are computed by the Sutherland law and the assumption of a constant Prandtl number. Perfect gas assumption is used in all flows considered in this paper.

For numerical simulations of flowfields over a curved body surface, structured body-fitted grids are used to transform the governing equations (1) in the Cartesian coordinates into a set of curvilinear three-dimensional coordinates (ξ,η,ζ,τ) along the body-fitted grid lines. The transformation relations for the two set of coordinates are

$$\begin{cases}\xi=\xi(x,y,z,t)\\ \eta=\eta(x,y,z,t)\\ \zeta=\zeta(x,y,z,t)\\ \tau=t\end{cases}\Longleftrightarrow\begin{cases}x=x(\xi,\eta,\zeta,\tau)\\ y=y(\xi,\eta,\zeta,\tau)\\ z=z(\xi,\eta,\zeta,\tau)\\ t=\tau\end{cases} \tag{8}$$

The governing equations (1) are transformed as follows:

$$\frac{1}{J}\frac{\partial U}{\partial\tau}+\frac{\partial E'}{\partial\xi}+\frac{\partial F'}{\partial\eta}+\frac{\partial G'}{\partial\zeta}+\frac{\partial E'_v}{\partial\xi}+\frac{\partial F'_v}{\partial\eta}+\frac{\partial G'_v}{\partial\zeta}+U\frac{\partial(1/J)}{\partial\tau}=0 \tag{9}$$

where

$$E'=(F_1\xi_x+F_2\xi_y+F_3\xi_z+U\xi_t)/J \tag{10}$$

$$F'=(F_1\eta_x+F_2\eta_y+F_3\eta_z+U\eta_t)/J \tag{11}$$

$$G'=(F_1\zeta_x+F_2\zeta_y+F_3\zeta_z+U\zeta_t)/J \tag{12}$$

$$E'_v=(F_{v1}\xi_x+F_{v2}\xi_y+F_{v3}\xi_z)/J \tag{13}$$

$$F'_v=(F_{v1}\eta_x+F_{v2}\eta_y+F_{v3}\eta_z)/J \tag{14}$$

$$G'_v=(F_{v1}\zeta_x+F_{v2}\zeta_y+F_{v3}\zeta_z)/J \tag{15}$$

where J is the Jacobian of the coordinate transformation and ξ_x, ξ_y, ξ_z, η_x, η_y, η_z, η_t, ζ_x, ζ_y, and ζ_z are the grid transformation matrices. In the equations the transformed inviscid fluxes E', F', and G' are standard flux terms with known eigenvalues and eigenvectors. The transport flux terms E'_v, F'_v, and G'_v contain both first-order and second-order spatial derivatives of velocity and temperature. These derivatives in the Cartesian coordinates (x,y,z) are transformed into the computational coordinates (ξ,η,ζ) using a chain rule for spatial discretization.

High-Order Semi-Implicit Method

In DNS of compressible boundary-layer flow, the governing equations are often solved by using the method of lines that the governing equations (9) are first discretized in space by a high-order finite difference method. The spatial discretization leads to a system of split ordinary differential equations, which can be solved by a semi-implicit time-stepping method.

In semi-implicit methods the spatial discretization of the Navier–Stokes equations is split into the stiff terms involving spatial derivatives normal to the wall and the rest of the flux terms. The split ordinary differential equation is then integrated in time using semi-implicit Runge–Kutta schemes derived by Zhong[7] or second-order AB-CN (Adams–Bashford and Crank–Nicolson) semi-implicit method. The resulting semi-implicit methods for computations of the Navier–Stokes equations are high-order accurate in both space and time and are much more efficient than explicit schemes because only the stiff terms in the equations are treated implicitly. For simplicity, only two-dimensional formulas of the high-order semi-implicit method are presented in the following sections. The extension to three-dimensional equations is straightforward.

Splitting of Governing Equations

The stiffness of viscous flow simulations is mainly a result of terms associated with derivatives in the wall-normal direction [$\partial(\,)/\partial\eta$ and $\partial^2(\,)/\partial\eta^2$] because of grid stretching near the wall. Therefore, Eq. (9) for a two-dimensional flow in (ξ,η,τ) is additively split into relatively nonstiff part $\boldsymbol{f}(U_{ij})$ and stiff part $\boldsymbol{g}(U_{ij})$ as follows:

$$\frac{1}{J}\frac{\partial U_{ij}}{\partial t}=\boldsymbol{f}(U_{ij})+\boldsymbol{g}(U_{ij}) \tag{16}$$

where

$$\boldsymbol{f}(U_{ij})=-\left[\frac{\partial E'}{\partial\xi}+\frac{\partial E'_v}{\partial\xi}+\frac{\partial F'_{v1}}{\partial\eta}+U\frac{\partial(1/J)}{\partial\tau}\right]_{ij} \tag{17}$$

$$\boldsymbol{g}(U_{ij})=-\left(\frac{\partial F'}{\partial\eta}+\frac{\partial F'_{v2}}{\partial\eta}\right)_{ij} \tag{18}$$

where i and j are the grid indices in the ξ and η direction, respectively. The transport flux vector in η direction F'_v is split into F'_{v2}, the part of the viscous flux terms only involving normal derivatives, and F'_{v1}, the part of the viscous flux terms except F'_{v2}, that is,

$$F'_v=F'_{v1}+F'_{v2} \tag{19}$$

Specifically, F'_v can be derived from Eq. (14) as

$$F'_v=\frac{E_v\eta_x+F_v\eta_y}{J}=\frac{1}{J}\begin{Bmatrix}0\\ \eta_x\tau_{11}+\eta_y\tau_{12}\\ \eta_x\tau_{21}+\eta_y\tau_{22}\\ \eta_x(\tau_{1k}u_k-q_1)+\eta_y(\tau_{2k}u_k-q_2)\end{Bmatrix} \tag{20}$$

where $k=1,2$. The transport terms, τ_{ij} and q_i given by Eqs. (6) and (7), can be transformed into (ξ,η) coordinates using the chain rule.

The F'_{v2} terms can then be obtained from Eq. (20) by picking out the η derivative terms. Then $\partial F'_{v2}/\partial\eta$ in Eq. (18) can be obtained as

$$\frac{\partial F'_{v2}}{\partial \eta} = \frac{1}{J}\begin{Bmatrix} 0 \\ \dfrac{\partial \tau_{\eta 2}}{\partial \eta} \\ \dfrac{\partial \tau_{\eta 3}}{\partial \eta} \\ \dfrac{\partial \tau_{\eta 4}}{\partial \eta} \end{Bmatrix} \tag{21}$$

where

$$\frac{\partial \tau_{\eta 2}}{\partial \eta} = \left(\frac{4}{3}\eta_x^2 + \eta_y^2\right)\left(\frac{\partial u}{\partial \eta}\frac{\mathrm{d}\mu}{\mathrm{d}T}\frac{\partial T}{\partial \eta} + \mu\frac{\partial^2 u}{\partial \eta^2}\right) + \frac{1}{3}\eta_y\eta_x\left(\frac{\partial v}{\partial \eta}\frac{\mathrm{d}\mu}{\mathrm{d}T}\frac{\partial T}{\partial \eta} + \mu\frac{\partial^2 v}{\partial \eta^2}\right)$$

$$\frac{\partial \tau_{\eta 3}}{\partial \eta} = \frac{1}{3}\eta_x\eta_y\left(\frac{\partial u}{\partial \eta}\frac{\mathrm{d}\mu}{\mathrm{d}T}\frac{\partial T}{\partial \eta} + \mu\frac{\partial^2 u}{\partial \eta^2}\right) + \left(\eta_x^2 + \frac{4}{3}\eta_y^2\right)\left(\frac{\partial v}{\partial \eta}\frac{\mathrm{d}\mu}{\mathrm{d}T}\frac{\partial T}{\partial \eta} + \mu\frac{\partial^2 v}{\partial \eta^2}\right)$$

$$\frac{\partial \tau_{\eta 4}}{\partial \eta} = \frac{\partial u}{\partial \eta}\tau_{\eta 2} + \frac{\partial v}{\partial \eta}\tau_{\eta 3} + u\frac{\partial \tau_{\eta 2}}{\partial \eta} + v\frac{\partial \tau_{\eta 3}}{\partial \eta} + \left(\eta_x^2 + \eta_y^2\right)\left[\frac{\mathrm{d}k}{\mathrm{d}T}\left(\frac{\partial T}{\partial \eta}\right)^2 + k\frac{\partial^2 T}{\partial \eta^2}\right]$$

where high-order finite difference methods are used to discretize both $\partial(\,)/\partial\eta$ and $\partial^2(\,)/\partial\eta^2$ terms.

In Eq. (16), $\boldsymbol{g}(U_{ij})$ is much stiffer than $\boldsymbol{f}(U_{ij})$ because grid spacing in the wall-normal direction is much smaller than that used in streamwise direction for most viscous flow simulations. Therefore, the high-order semi-implicit method is used to overcome the stiffness of $\boldsymbol{g}(U_{ij})$ while maintaining high-order temporal accuracy.

Spatial Discretization

The split governing equation (16) is first approximated by high-order-accurate finite difference methods. For the case of DNS of compressible boundary layers with a bow shock, the shock wave can be treated by a shock-fitting method because there is no discontinuity in the interior of the computational domain. In this paper a fifth-order upwind scheme[8] is used to discretize the inviscid flux derivatives. Meanwhile, high-order central difference schemes, such as the sixth-order central scheme, are used to discretize the viscous flux terms in the equations.

For the inviscid flux vectors in the Eqs. (17) and (18), the flux Jacobians contain both positive and negative eigenvalues in general. A local Lax–Friedrichs scheme is used to split the inviscid flux vectors into positive and negative wave fields. As discussed in Ref. 8, the Lax–Friedrichs scheme is dissipative for a low-order scheme, but for a high-order scheme it performs very well. As a result, the flux term F' in Eq. (18) can be split into two terms of pure positive and negative eigenvalues as follows:

$$F' = F'_+ + F'_- \tag{22}$$

where

$$F'_+ = \tfrac{1}{2}(F' + \lambda U) \tag{23}$$

$$F'_- = \tfrac{1}{2}(F' - \lambda U) \tag{24}$$

where λ is chosen to be larger than the local maximum eigenvalues of F':

$$\lambda = (|\nabla\eta|/J)\left[\sqrt{(\epsilon c)^2 + u'^2} + c\right] \tag{25}$$

where

$$u' = \frac{\eta_x u + \eta_y v + \eta_z w + \eta_t}{|\nabla\eta|} \tag{26}$$

and the parameter ϵ is a small positive constant added for the smoothness of the splitting. The fluxes F'_+ and F'_- contain only positive and negative eigenvalues, respectively. Therefore, in the spatial discretization of Eq. (17), the flux derivatives are split into two terms:

$$\frac{\partial F'}{\partial \eta} = \frac{\partial F'_+}{\partial \eta} + \frac{\partial F'_-}{\partial \eta} \tag{27}$$

where the first term on the right-hand side is discretized by an upwind high-order finite difference method and the second term is discretized by a downwind high-order finite difference method. The fifth-order upwind explicit scheme[8] for the derivative of a variable ϕ is

$$\left(\frac{\partial \phi}{\partial \eta}\right)_j = \frac{1}{60h}\sum_{k=-3}^{3} a_{j+k}\phi_{j+k} \tag{28}$$

where $a_{j\pm 3} = \pm 1 + \frac{1}{12}\alpha$, $a_{j\pm 2} = \mp 9 - \frac{1}{2}\alpha$, $a_{j\pm 1} = \pm 45 + \frac{5}{4}\alpha$, and $a_j = -\frac{5}{3}\alpha$. This scheme is a fifth-order upwind scheme when $\alpha < 0$ ($\alpha = -2$). The scheme reduces to a sixth-order central scheme when $\alpha = 0$. Meanwhile, the corresponding sixth-order central explicit inner scheme for the second-order spatial derivative in the viscous term is

$$\left(\frac{\partial^2 \phi}{\partial \eta^2}\right)_j = \frac{\phi_{j-3} - \frac{17}{2}\phi_{j-2} + 135\phi_{j-1} - 245\phi_j + 135\phi_{j+1} - \frac{17}{2}\phi_{j+2} + \phi_{j+3}}{90h^2} \tag{29}$$

The spatial discretization of the split Eq. (16) using these high-order schemes coupled with appropriate boundary conditions leads to a system of ordinary differential equations in the form of

$$\frac{\mathrm{d}\boldsymbol{u}}{\mathrm{d}t} = [\boldsymbol{f}(t, \boldsymbol{u})] + [\boldsymbol{g}(t, \boldsymbol{u})] \tag{30}$$

where $\boldsymbol{u} = \{U_{ij} \text{ for } i = 1, \ldots IL,\ j = 1, \ldots JL\}$ is the vector of all discretized variables in the flowfield; $[\boldsymbol{f}(t, \boldsymbol{u})]$ represents the discretized nonstiff term; and $[\boldsymbol{g}(t, \boldsymbol{u})]$ represents the discretized stiff term.

Semi-Implicit Time-Stepping Schemes

The system of ordinary differential equations of Eq. (30) can be integrated in time using semi-implicit temporal schemes, where $[\boldsymbol{f}(t, \boldsymbol{u})]$ is treated explicitly and $[\boldsymbol{g}(t, \boldsymbol{u})]$ is treated implicitly. Second-order AB-CN semi-implicit method and semi-implicit Runge–Kutta schemes derived by Zhong[7] and Yoh and Zhong[9] are used in this paper.

The AB-CN method is

$$\boldsymbol{u}^{n+1} = \boldsymbol{u}^n + (h/2)[3\boldsymbol{f}(\boldsymbol{u}^n) - \boldsymbol{f}(\boldsymbol{u}^{n-1})] + (h/2)[\boldsymbol{g}(\boldsymbol{u}^n) + \boldsymbol{g}(\boldsymbol{u}^{n+1})] \tag{31}$$

where h is the size of the time step. The AB-CN method is simple, but it is only second-order accurate. It was shown by Zhong[7] that in order to have a third- or higher-order temporal accuracy the semi-implicit method needs to be derived in a way that the effects of coupling between the implicit and explicit terms on the accuracy need to be considered. Zhong[7] subsequently derived three kinds of third-order semi-implicit Runge–Kutta schemes for high-order temporal integration of the governing equations for reacting flow simulations. High-order, low-storage semi-implicit Runge–Kutta method versions (LSSIRK) have also been derived in Ref. 9. In particular, the

Rosenbrock-typeRunge–Kutta (LSSIRK-rC) method can be written as follows:

$$\begin{cases} [\boldsymbol{I} - hc_j \boldsymbol{J}(\boldsymbol{u}_{j-1} + \bar{c}_j \boldsymbol{k}_{j-1})]\boldsymbol{k}_j = h[\boldsymbol{f}(\boldsymbol{u}_{j-1}) + \boldsymbol{g}(\boldsymbol{u}_{j-1} \\ \quad + \bar{c}_j \boldsymbol{k}_{j-1})] + a_j[\boldsymbol{I} - hc_j \boldsymbol{J}(\boldsymbol{u}_{j-1} + \bar{c}_j \boldsymbol{k}_{j-1})]\boldsymbol{k}_{j-1} \\ \boldsymbol{u}_j = \boldsymbol{u}_{j-1} + b_j \boldsymbol{k}_j \end{cases} \tag{32}$$

where $j = 1, \ldots, r$ and parameters c_j, $\bar{c}_j$, b_j can be found in Ref. 9. For instance, in LSSIRK-3C, $b_1 = \frac{1}{4}$, $b_2 = \frac{2}{9}$, $b_3 = 3$, $a_1 = -\frac{1}{4}$, $a_2 = -\frac{29}{27}$, $c_1 = 2.26760$, $c_2 = 2.68530$, $c_3 = 2.30975$, $\bar{c}_2 = -1.14310$, and $\bar{c}_3 = -2.03122$. The parameters of the semi-implicit Runge–Kutta methods are chosen by both stability and accuracy requirements with the simultaneous coupling between the explicit and implicit terms. In this paper, except for the AB-CN method, there are three kinds of semi-implicit Runge–Kutta methods to be used to advance the spatial discretization of Navier–Stokes equations in time. They are the first-order semi-implicit Runge–Kutta scheme (ASIRK-1C); the second-order, low-storage semi-implicit Runge–Kutta scheme (LSSIRK-2C); and the third-order, low-storage semi-implicit Runge–Kutta scheme (LSSIRK-3C).

In applying the semi-implicit method to Navier–Stokes equation (30), the global Jacobian matrix comes from the implicit method and can be defined by $\boldsymbol{J}(\boldsymbol{u}) = \partial \boldsymbol{g}/\partial \boldsymbol{u}$. The components of the Jacobian $\boldsymbol{J}(\boldsymbol{u})$ are derived by considering the variation of $\boldsymbol{g}(U_{ij})$ in Eq. (16):

$$\delta \boldsymbol{g}(U_{ij}) = \delta\left(-\frac{\mathrm{D}F'_+}{\mathrm{D}\eta} - \frac{\mathrm{D}F'_-}{\mathrm{D}\eta} - \frac{\mathrm{D}F'_{v2}}{\mathrm{D}\eta}\right)_{ij} \tag{33}$$

where $\mathrm{D}/\mathrm{D}\eta$ is the fifth-order finite difference approximation of the derivatives in the wall-normal direction and F'_+, F'_- are inviscid fluxes given by Eq. (27). The variations for these inviscid fluxes are

$$\delta F'_{\pm}(U) = \frac{\partial\left[\frac{1}{2}(F' \pm \lambda U)\right]}{\partial U}\delta U \tag{34}$$

and those for the viscous flux are

$$\delta F'_{v2} = \boldsymbol{A}_v \frac{\partial^2}{\partial \eta^2}(\boldsymbol{M}\delta U) + \boldsymbol{B}_v \frac{\partial}{\partial \eta}(\boldsymbol{M}\delta U) + \boldsymbol{C}_v(\boldsymbol{M}\delta U) \tag{35}$$

where the matrices $\boldsymbol{M}$, $\boldsymbol{A}_v$, $\boldsymbol{B}_v$, and $\boldsymbol{C}_v$ are given in the Appendix. Substituting Eqs. (34) and (35) into Eq. (33), where the derivatives are approximated by the fifth-order upwind scheme and sixth-order central scheme described in Eqs. (28) and (29), leads to

$$\begin{aligned} \delta \boldsymbol{g}(U_{ij}) = {} & \boldsymbol{A}_{ij}\delta U_{ij-3} + \boldsymbol{B}_{ij}\delta U_{ij-2} + \boldsymbol{C}_{ij}\delta U_{ij-1} + \boldsymbol{D}_{ij}\delta U_{ij} \\ & + \boldsymbol{E}_{ij}\delta U_{ij+1} + \boldsymbol{F}_{ij}\delta U_{ij+2} + \boldsymbol{G}_{ij}\delta U_{ij+3} \end{aligned} \tag{36}$$

where the coefficient matrices are given in the Appendix.

The final global Jacobian matrix for the system of ordinary differential equations, Eq. (30), is a block seven-diagonal matrix involving terms along the j grid direction only. This block seven-diagonal system of equations can be solved efficiently by a banded matrix solver.

Boundary Conditions

The physical boundary conditions for viscous flows are nonslip conditions for velocity and isothermal or adiabatic condition for temperature. The freestream flow conditions are specified by a given flow. The disturbances such as planar acoustic waves imposed into the flow are specified according to their own particular physical nature.

For numerical simulations it is necessary to set numerical boundary conditions for some flow variables in addition to the physical boundary conditions. This is especially the case at the computational boundary of the exit and inlet. There have been many investigations on the issues of numerical boundary conditions for the direct numerical simulations of compressible as well as incompressible boundary layers. Examples of the work include the following: Orszag et al.[10] presented a sponge layer with absorbing boundary conditions in the study of problems involving wave propagation, Streett and Macaraeg[11] proposed a buffer domain in the outflow boundary for unsteady transition-to-turbulence simulations, Poinsot and Lele[12] discussed characteristic-based boundary conditions for direct simulation of compressible viscous flows, and Guo et al.[6] compared the results obtained by using the preceding different boundary conditions in the simulation of compressible boundary-layer transition. Collis and Lele[13] studied the problem of compressible swept leading-edge receptivity by using inflow sponge and outflow sponge boundary conditions.

Because the emphasis of current paper is the semi-implicit method for efficient and accurate time integration of the governing equations, we will mainly consider flows either with periodic boundary conditions or with a supersonic exit where the reflection of disturbances are negligible. Boundary conditions on the wall are included in the global Jacobian matrix to ensure that it is a global implicit equation and advanced in time. For example, to include the lower wall boundary conditions, by imposing the fourth-order boundary conditions δU_{i1} can be written as

$$\begin{aligned} \delta U_{i1} = {} & \left(\frac{\partial U}{\partial V}\right)_{i1}\left(\frac{\partial V_{i1}}{\partial V_{i2}}\right)\left(\frac{\partial V}{\partial U}\right)_{i2}\delta U_{i2} \\ & + \left(\frac{\partial U}{\partial V}\right)_{i1}\left(\frac{\partial V_{i1}}{\partial V_{i3}}\right)\left(\frac{\partial V}{\partial U}\right)_{i3}\delta U_{i3} \\ & + \left(\frac{\partial U}{\partial V}\right)_{i1}\left(\frac{\partial V_{i1}}{\partial V_{i4}}\right)\left(\frac{\partial V}{\partial U}\right)_{i4}\delta U_{i4} \\ & + \left(\frac{\partial U}{\partial V}\right)_{i1}\left(\frac{\partial V_{i1}}{\partial V_{i5}}\right)\left(\frac{\partial V}{\partial U}\right)_{i5}\delta U_{i5} \end{aligned} \tag{37}$$

where V and $\partial V/\partial U$ can be found in Appendix and $(\partial V_{i1}/\partial V_{ij})(j = 2, \ldots, 5)$ are the coefficients of the corresponding boundary conditions applied to the lower wall.

Numerical Results

To test the usefulness and accuracy of the new algorithm, the new high-order semi-implicit schemes with a high-order shock-fitting algorithm for hypersonic flow over a blunt body have been extensively validated and evaluated. The shock-fitting procedure can be turned off if there is no shock in the flowfield. The main issue of the evaluation is the temporal accuracy of the implicit-explicit splitting in the high-order simulations and the efficiency of the semi-implicit schemes compared to explicit schemes for transient viscous flow simulations. In the following sections stability of supersonic Couette flow is simulated by using the new high-order semi-implicit method to test the accuracy and efficiency of the new method. Subsequently, stability of supersonic boundary layer is studied. Finally, two-dimensional hypersonic boundary-layer flow over a blunt body is validated.

Stability of Two-Dimensional Supersonic Couette Flow

The new high-order semi-implicit scheme is applied to the simulation of the two-dimensional compressible Navier–Stokes problem of temporal stability of supersonic Couette flow. Compressible Couette flow is a wall-bounded parallel shear flow whose steady mean flow can be obtained accurately by a shooting method. Because the mean flow is parallel, the temporal linear stability analysis on the full Navier–Stokes equations can be obtained when disturbance is weak.[8] Therefore, we can test the semi-implicit method in computing both steady and unsteady two-dimensional supersonic Couette flow by comparing the numerical solutions with exact transient solutions obtained from the analysis based on linear stability theory (LST).

Steady Flow Solutions

We first use the high-order semi-implicit codes for unsteady Navier–Stokes equations to compute the steady solutions of the supersonic Couette flow. The results are compared with the "exact" solutions obtained by a shooting method. Several cases with different Mach numbers, Reynolds numbers, and wall temperature have been tested. The results of only one of the cases are shown in this paper. The flow conditions are $M_\infty = 2$ and the upper wall is an

Table 1 Numerical errors for computations of supersonic Couette flow using fifth-order semi-implicit scheme ($e_1 = \|e\|_1$ and $e_2 = \|e\|_2$)

Grid	$e_1 \times 10^{-6}$	Ratio	$e_2 \times 10^{-6}$	Ratio
50	6.9913	——	1.4114	——
100	0.2315	30.2	0.034	41.5

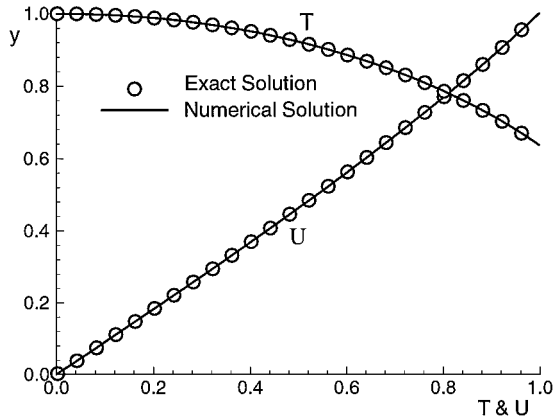

Fig. 1 Dimensionless temperature and velocity profiles for a Mach 2 Couette flow.

isothermal wall with $T_\infty = 220.66667$ K, whereas the lower wall is an adiabatic wall. The gas is assumed to be perfect gas with $\gamma = 1.4$ and $Pr = 0.72$. The viscosity coefficient is calculated by Sutherland's law. To calculate the steady flow of supersonic Couette flow, the semi-implicit method ASIRK-1C is simplified to the fully implicit method because the mean flow is parallel in the horizontal direction. At this time, because the temporal accuracy is not our important concern, very large Δt is used in the ASIRK-1C method with a Courant–Friedrichs–Lewy (CFL) number 10^5.

Figure 1 shows the steady nondimensional velocity and temperature profiles obtained by using the semi-implicit fifth-order upwind scheme with 100 uniform grid points. Velocity is nondimensionalized by the velocity at the upper wall, and temperature is nondimensionalized by T_∞. The numerical results agree well with the exact solutions. The accuracy of the numerical simulations is evaluated by grid-refinement studies using several sets of uniform grids. The quantitative numerical errors of the simulations using two kinds of uniform grids are listed in Table 1. The table shows that the numerical errors for this fifth-order semi-implicit scheme in spatial discretization are of the order of 10^{-6} using 50 grid points and 2.315×10^{-7} using 100 grid points in a wall-normal direction. The theoretical ratio of the errors between the coarse grids and the fine grids is 32 for a fifth-order scheme. The results in Table 1 show that the numerical algorithms are able to maintain high-order accuracy in spatial discretization.

Unsteady Flow Solutions

Three different kinds of semi-implicit schemes, ASIRK-1C, LSSIRK-2C, and LSSIRK-3C, are subsequently tested by doing numerical simulations for the temporal stability of the same steady two-dimensional compressible Couette flow. The temporal stability problems are concerned with the growth or decay of some superimposed spatially periodic disturbances on the steady Couette flow solutions. The small initial disturbances, which are periodic in the x direction, are in the form of eigenfunctions obtained from linear stability analysis:

$$q'(x, y, t) = \hat{q}(y) \exp[i(\alpha x - \omega t)] \tag{38}$$

where α (real number) is a given wave number and complex frequency ω and eigenfunction $\hat{q}(y)$ are both obtained by the stability analysis; $q'(x, y, t)$ is the disturbance of any flow variable. The disturbances will grow or decay exponentially if the sign of the imaginary part of ω is positive or negative, respectively.

In the numerical simulations the developments of these initial disturbances in the two-dimensional flowfield are computed using the full Navier–Stokes equations. The initial conditions are the steady flow solutions plus disturbances given by a set of eigenfunctions obtained by linear stability analysis[14] as follows:

$$u(x, y, t = 0) = \bar{u} + \epsilon Re\{\hat{u}(y) \exp[i(\alpha x - \omega t)]\} \tag{39}$$

where ϵ is the magnitude of the disturbance.

The unsteady flowfield is solved by computing the unsteady Navier–Stokes equations using different kinds of implicit temporal discretizations. The same stretched grids are used in the y direction as those used in the linear stability theory calculations. The computational domain in the simulation is one period in length in the x direction, and periodic boundary conditions are used. The numerical accuracy of the semi-implicit schemes is evaluated using analytical solutions obtained from the linear stability analysis.[14]

The initial disturbance of the test case is chosen to be a stable mode according to the linear stability theory. The flow conditions are $M_\infty = 2$ and $Re_\infty = 10^3$. The initial disturbance wave has a dimensionless wave number of $\alpha = 3$, which is nondimensionalized by the distance between two plates, and the eigenvalue obtained from the temporal linear stability analysis is $\omega = \omega_r + \omega_i i = 5.52034015848 - 0.132786378788i$, where a negative ω_i means that the disturbances will decay in time with a dimensionless frequency ω_r. The magnitude of the disturbances ϵ is 0.002. Figure 2 shows the contour of the real part of the eigenfunciton of p' in the flowfield obtained by linear stability analysis. To evaluate the temporal accuracy and efficiency of the semi-implicit schemes for unstable flow simulations, the unsteady two-dimensional supersonic Couette flow is computed by using four kinds of time-stepping methods, which are first-order explicit temporal discretization, ASIRK-1C, LSSIRK-2C, and LSSIRK-3C, respectively. The spatial scheme is the same fifth-order scheme described in Eq. (28). In the simulation a set of 52×101 stretching grids is used. The explicit and semi-implicit methods use different time steps according to the stability restriction. The actual values of CFL number used in the simulations are given in Table 2.

Figure 3 shows the comparison of the numerical results using the LSSIRK-2C method and the linear stability theory predictions for the time history of velocity perturbations perturbations, respectively, at a fixed point in the two-dimensional supersonic Couette

Table 2 Efficiency comparison for the simulations of temporal stability of supersonic Couette flow ($M_\infty = 2.0$, $Re = 10^3$, run to 4.22837×10^{-3} s)

Parameter or scheme	Explicit method	Semi-implicit method	Ratio
CFL number	0.0043	0.33	——
$\Delta x/\Delta y$	202.95	202.95	——
Numer of time steps	226,116	3,000	75.372
CPU time consumed, s			
Explicit	60,456.63	——	——
ASIRK-1C	——	3,518.96	17.1802
LSSIRK-2C	——	7,144.83	8.4616
LSSIRK-3C	——	11,541.26	5.2383

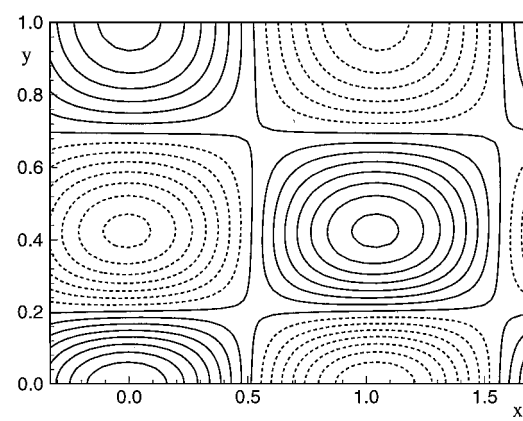

Fig. 2 Wave patterns of $Re\{p'\}$ with $\omega = 5.520340158 - 0.132786378i$.

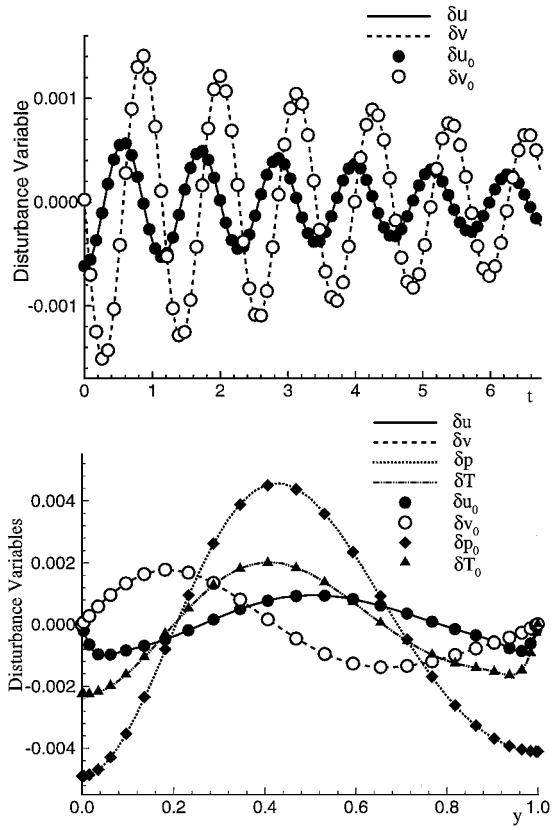

Fig. 3 Comparisons of velocity perturbation time history and distributions in the y direction (LST: δu_0, δv_0, δp_0, δT_0; DNS: δu, δv, δp, δT).

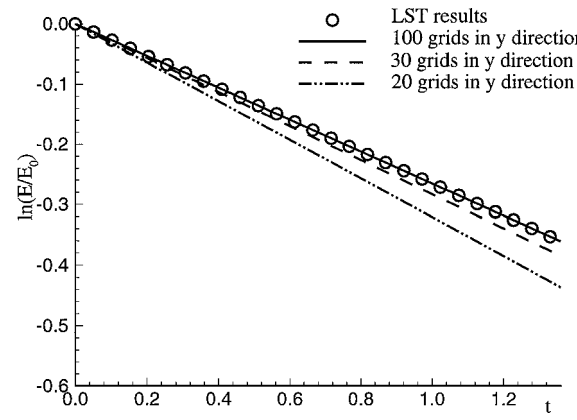

Fig. 4 Computed perturbation energy using different grid numbers in the y direction.

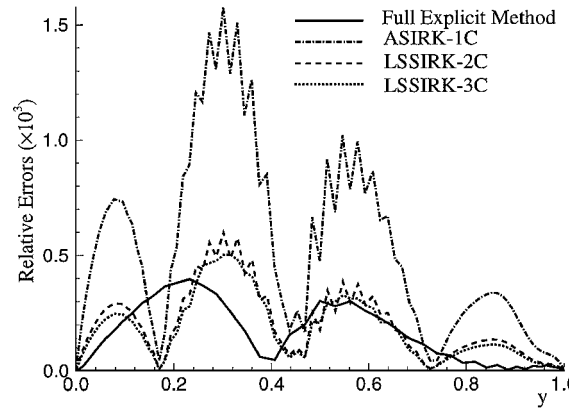

Fig. 5 Comparisons of relative errors among different numerical methods.

flowfield and the comparison of the distribution of instantaneous flow perturbations in the y direction after about six wave periods. The results show that the two-dimensional numerical simulations of the Navier–Stokes equations for the stability of supersonic Couette flow by using semi-implicit method agree well with the results from linear stability theory.

The amplitudes of the disturbance waves decay as a function of time in this case. For sufficiently low-amplitude waves, linear stability analysis shows that the perturbation kinetic energy of the solutions is

$$E(t) = \int\int \frac{1}{2}(u'^2 + v'^2)\,\mathrm{d}x\,\mathrm{d}y = E_0 e^{2\omega_i t} \tag{40}$$

where E_0 is the perturbation energy at $t = 0$. Figure 4 displays the time history of $\ln[E(t)/E_0]$ for the computed perturbation energy and the analytical value of the linear stability analysis in one wave period, which is equal to $2\omega_i$. Different grid numbers in the y direction are used to study the required grids by accuracy requirement. The numerical results using 100 grid points in the y direction agree well with the linear stability results. However, the numerical errors are accumulated along the time when fewer grids, 20 and 30 grids, are used in the y direction.

To evaluate the temporal accuracy of the semi-implicit schemes at different orders, Fig. 5 shows the relative errors for the solutions in the y direction for four kinds of numerical methods at the end of two wave periods. Each method uses different size of time step Δt according to the stability restriction of each individual method. Consequently, the explicit method uses smaller Δt in every time step because of stability constraint and is not efficient in computational time. On the other hand, much larger Δt can be used for semi-implicit methods so that the computational time can be reduced. However, it is necessary to ensure that temporal accuracy is not reduced because of the lager Δt. Figure 5 shows that the explicit method has small errors even for the first-order explicit temporal discretization. The errors for the explicit scheme are mainly caused by those from the spatial discretization while very small Δt is used. The semi-implicit method, on the other hand, loses some accuracy when first-order temporal discretization is used because a larger Δt is used in every time step. As the temporal orders of the semi-implicit methods increased to second and third order, the relative errors of the semi-implicit methods were close to those of explicit method; even the time step was much larger. This is because the relative errors for the second-order and third-order semi-implicit methods are mainly caused by the numerical errors from the spatial discretization. The temporal accuracy are ensured for both second-order and third-order semi-implicit methods using large Δt with CFL number 0.33.

Table 2 compares the computational efficiency using the explicit method and the semi-implicit methods by simulating the flow about two wave periods and records the real CPU time consumed by each method. Table 2 shows that the time-step ratio of the explicit method and the semi-implicit methods is about 75.4. Therefore, though it takes more CPU time to advance the semi-implicit method per time step, the overall CPU time is much smaller than that used by the explicit method. Specifically, the explicit method requires about 8.5 and 5.2 times more CPU time than the second-order and third-order semi-implicit methods, respectively, to do the same simulation with the same accuracy. Therefore, the overall computational efficiency is improved while the temporal accuracy of transient flow simulation is maintained by using second-order and third-order semi-implicit methods. Considering the computation accuracy and efficiency together, the second-order semi-implicit method is the preferred method in this paper.

Stability of Two-Dimensional Supersonic Boundary Layers

Compared with the supersonic Couette flow, the supersonic boundary layer is a test case that is closer to practical wall-bounded high-speed viscous flow. The fifth-order semi-implicit schemes for unsteady Navier–Stokes equations are applied to simulate the temporal stability of supersonic flat-plate boundary layer. In this test case the semi-implicit method contains both explicit and implicit treatment in the x and y directions, respectively. The initial

conditions are the steady boundary-layer flow solutions plus disturbances given by a set of eigenfunctions obtained by linear stability analysis. The flow conditions are $M_\infty = 4.5$ and Reynolds number $Re = 10^3$ (based on the boundary-layer thickness).

The computation uses 42×141 grids covering a section of the boundary layer. The grids are stretched in the y direction in order to resolve the high shear layer in the boundary layer. Based on the results of the accuracy assessment in simulating stability of supersonic Couette flow, the LSSIRK-2C semi-implicit method is used as the time-stepping method. The grid has an aspect ratio of $\Delta x/\Delta y = 169.2857$.

Again, the numerical methods are first tested in steady mean flow computations. Figure 6 displays the mean flow of numerical results compared with the exact solutions obtained by solving the boundary-layer equations using a shooting method with several orders of magnitude smaller errors. The numerical results agree well with the exact solutions.

The unsteady flow simulations are carried out by choosing the initial disturbance wave number $\alpha = 0.22$, which is nondimensionalized by boundary-layer thickness δ. The eigenvalue obtained from the temporal linear stability analysis is $\omega = \omega_r + \omega_i i = 25.77363556598 + 0.2497128329918i$. The disturbances are amplified with time because of a positive ω_i. In the temporal simulations of the growth of the initial disturbances in the boundary layer, the periodic boundary condition is used for the disturbances in the x direction. The magnitude ϵ of the disturbances is 0.004. The numerical results are compared with results from linear stability analysis.

Figure 7 shows the comparison of the DNS results and the LST predictions for the time history of velocity perturbations at a fixed point in the two-dimensional supersonic flat-plate boundary layer. The DNS results and the LST predictions agree very well. Similar to the test case of supersonic Couette flow, comparisons of the time history of $\ln[E(t)/E_0]$ for the computed perturbation energy by

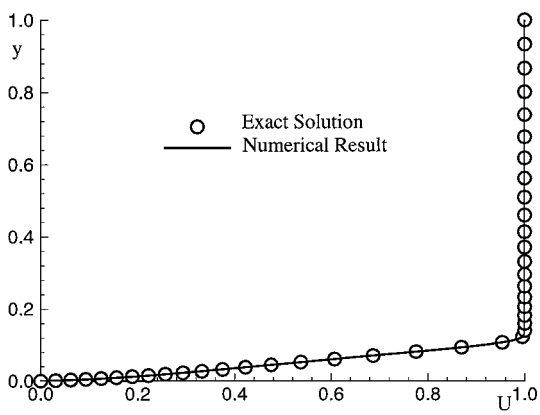

Fig. 6 Comparisons of velocity profiles of flat-plate boundary-layer flow.

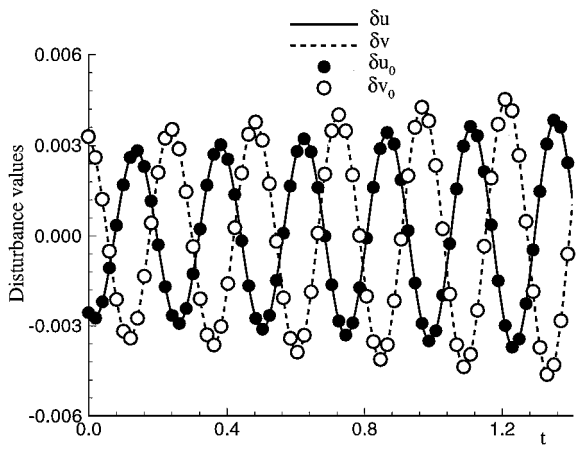

Fig. 7 Comparisons of velocity perturbation time history (LST: δu_0, δv_0; DNS: δu, δv).

Table 3 Efficiency comparison for the simulations of temporal stability of supersonic flat-plate boundary layer ($M_\infty = 4.5$, run to 1.074×10^{-3} s)

Parameter	Explicit method	LSSIRK-2C method	Ratio
CFL number	0.00284	0.18	——
$\Delta x/\Delta y$	169.2857	169.2857	——
Number of time steps	126,702	2,000	63.351
CPU time, s	39,809.77	6,184.35	6.437

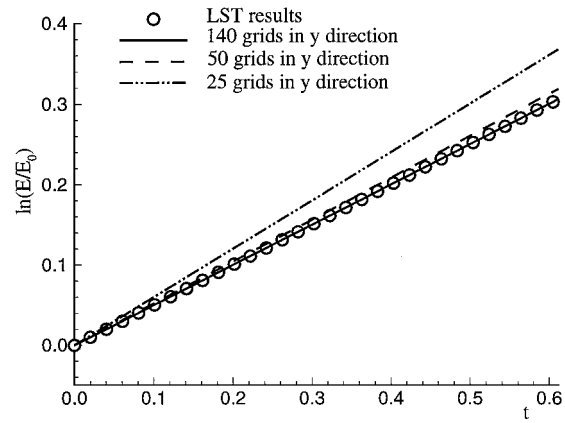

Fig. 8 Computed perturbation energy using different grid numbers in the y direction.

using different grid numbers in the y direction are shown in Fig. 8. The numerical results obtained by using 140 grids in the y direction agree well with the linear stability results. When fewer grids such as 50 and 25 grids are used in the y direction, the numerical errors are accumulated along the time.

The efficiency of the semi-implicit method is evaluated, and the results are shown in Table 3. Compared with the CFL number 0.00284 used by the explicit method, a larger CFL number 0.18 can be used by the semi-implicit method. The ratio of CPU time required by the explicit method and the semi-implicit method to advance the simulations about two wave periods is about 6.4. Therefore, the overall computational efficiency can be improved by using a semi-implicit method.

Receptivity of Hypersonic Flow over a Parabola

The last test is the numerical simulation of the receptivity of a two-dimensional boundary layer to weak freestream acoustic disturbance waves for hypersonic flow past a parabolic leading edge at zero angle of attack. The same problem is studied in details using explicit method by Zhong in Ref. 8. In this paper the same flow conditions and boundary conditions as those in Ref. 8 are used to evaluate the numerical efficiency and accuracy of the new high-order semi-implicit method.

In the receptivity simulation the unsteady motions of the bow shock caused by freestream disturbances are treated by a shock-fitting method as a computational boundary. The steady flowfield is first obtained by computing the flow without freestream waves. The unsteady simulation is then carried out by superimposing a freestream disturbances on the steady mean flow solutions. The subsequent development of disturbance waves in the boundary layer with the effects of the bow-shock interaction is simulated by computing the full Navier–Stokes equations. The freestream disturbances are assumed to be weak monochromatic planar acoustic waves with wave front normal to the center line of the body. The perturbations of flow variable introduced by the freestream acoustic wave before reaching the bow shock can be written in the following form:

$$\{u', v', p', \rho'\}_\infty = \{|u'|, |v'|, |p'|, |\rho'|\}_\infty \exp[i(kx - \omega t)] \quad (41)$$

where $|u'|$, $|u'|$, $|p'|$, and $|\rho'|$ are dimensionless perturbation amplitudes satisfying $|u'|_\infty = \epsilon$, $|v'|_\infty = 0$, $|p'|_\infty = \gamma M_\infty \epsilon$, and $|\rho'|_\infty = M_\infty \epsilon$, where ϵ is a small number representing the freestream wave magnitude. The parameter ω is the freestream circular frequency.

The corresponding dimensionless frequency F is defined as $F = \omega^* \nu^* / U_\infty^{*2} = \omega / Re_\infty$.

The specific two-dimensional test case is a Mach 15 flow over a two-dimensional parabolic body, which surface is given by $x^* = b^* y^{*2} - d^*$, where b^* is a given constant and d^* taken as the reference length. The body surface is assumed to be a nonslip wall with an isothermal wall temperature T_w^*. The specific flow conditions are $M_\infty = 15$, $\epsilon = 5 \times 10^{-4}$, $T_\infty^* = 192.989$ K, $p_\infty^* = 10.3$ Pa, $T_w^* = 1000$ K, $\gamma = 1.4$, $R^* = 286.94$ Nm/kgK, $Pr = 0.72$, $b^* = 40\ \mathrm{m}^{-1}$, $d^* = 0.1$ m, $T_r^* = 288$ K, $T_s^* = 110.33$ K, $\mu^* = 0.17894 \times 10^{-4}$ kg/ms, and $Re_\infty = \rho_\infty^* U_\infty^* d^* / \mu_\infty^* = 6026.55$.

The steady flow solutions of the Navier–Stokes equations for the viscous hypersonic flow over the parabola are first obtained by using second-order AB-CN semi-implicit temporal discretization instead of LSSIRK-2C temporal discretization because the AB-CN method is easier to program for the problem with shock-fitting method and has fewer computation steps than the LSSIRK-2C. Meanwhile, AB-CN has second-order temporal accuracy, which is the same as the LSSIRK-2C method. LSSIRK-3C is used for third-order temporal discretization. In this paper only the results using the AB-CN method are presented. On the other hand, fifth-order spatial discretization is implemented, and the solutions are advanced to a steady state without freestream perturbations. The calculations are carried out by using a set of 160×120 grids. The use of the semi-implicit method makes it possible to use a larger time step measured by the larger CFL number used in the simulations. In steady flow simulation the CFL number used by the semi-implicit method is 0.15 depending on Δx. This is much larger than the CFL number 0.0049 used by the explicit simulations.

Having obtained the steady solutions, the unsteady simulations are carried out for the generation of boundary-layer instability waves by introducing freestream planar acoustic disturbances wave with a dimensionless frequency $F \times 10^{-6} = 2655$. The numerical solutions are obtained by using a high-order semi-implicit method with a set of 160×120 grids. To maintain the temporal accuracy in unsteady simulations, the CFL number is used as 0.14 based on Δx compared with CFL number 0.0047 used by the explicit method. The unsteady computations are run for more than 29 periods in time to ensure that periodic solutions have been reached for the entire flowfield. Efficiency and accuracy of the new semi-implicit method are studied for this unsteady receptivity problem.

Figure 9 shows the contours for the instantaneous perturbation u' of the velocity in the x direction after the flowfield has reached a periodic state and the amplitude $|u'|$ of the disturbances. The instantaneous contours of u' show the development of instability waves in the boundary layer on the surface. The first region of $x < 0.2$ dominated by the first mode instability and the second region of $x > 0.2$ dominated by the second mode instability are numerically obtained by using the semi-implicit method. The characteristics of the switching of instability modes from region 1 to region 2, the decay of the first mode and the growth of the second mode with the sudden phase angle change near the body surface around $x = 0.2$, which have been discussed in Ref. 8 by using the high-order explicit method, are obtained, too. The accuracy of the unsteady solutions obtained by using the new semi-implicit method with much larger CFL number is assessed by comparison with the explicit solutions.

Figure 10 compares the distribution of instantaneous entropy perturbations along the parabola surface. The results show a very good agreement between results of the semi-implicit method and those of the explicit method. Table 4 shows the real consumed CPU time comparison between the explicit method and the

Table 4 Efficiency comparison for the simulations of the receptivity of hypersonic flow over a parabola ($M_\infty = 15$, run to 1.0091×10^{-3} s)

Parameter	Explicit method	AB-CN method	Ratio
CFL number	0.0047	0.14	——
Grid	160×120	160×120	——
$\Delta x / \Delta y$	245.82	245.82	——
Number of time steps	446,811	15,000	29.787
CPU time, s	213,037.47	24,437.55	8.718

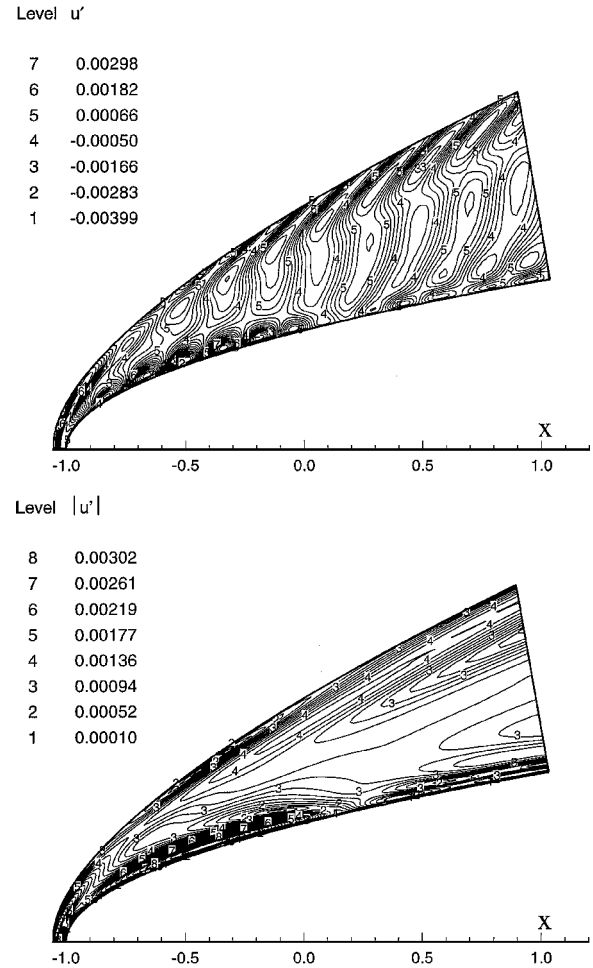

Fig. 9 Instantaneous u' (top) and the Fourier amplitude $|u'|$ contours (bottom).

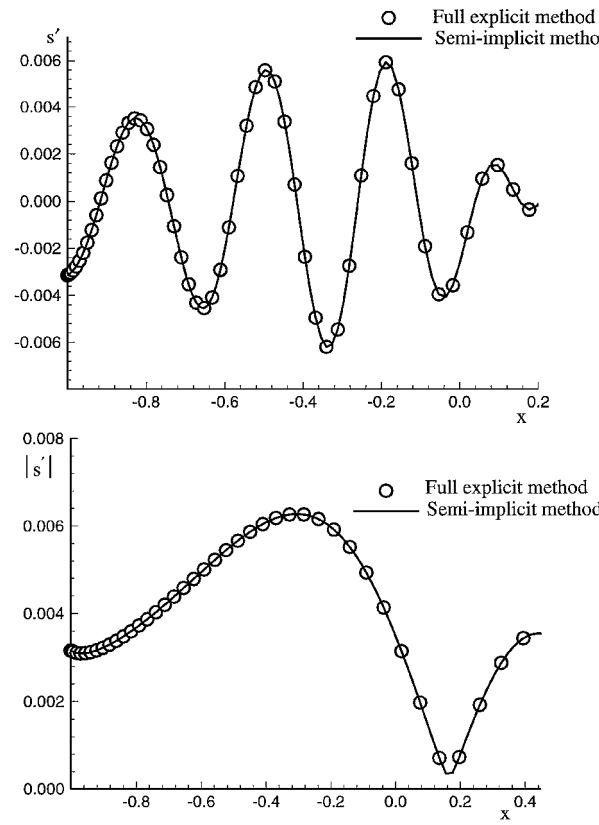

Fig. 10 Comparisons of computed entropy perturbations s' (top) and the Fourier amplitude $|s'|$ (bottom).

second-order AB-CN semi-implicit method. The real consumed CPU time is recorded by running the code about 10 wave periods. The computation results show that the new schemes improve the computational efficiency by nearly one order of magnitude compared with the explicit method. In this case the magnitude of the maximum time step used in numerical calculation is limited by the stability conditions related to the grid size in the streamwise direction only. The results demonstrate that stiffness of fine grids in the direction across the boundary layers has been removed by the semi-implicit method while the temporal accuracy of the unsteady simulations has been maintained. Accuracy and efficiency are well approached for the simulations of unsteady compressible flows by using the high-order semi-implicit method.

Conclusions

An efficient and high-order-accurate semi-implicit method has been presented in this paper for the DNS of unsteady compressible flows based on the unsteady Navier–Stokes equations. The method uses semi-implicit treatment to overcome the stiffness of viscous wall-normal derivative terms, whereas the streamwise terms are computed by the explicit method for efficient unsteady flow calculations. The efficiency and accuracy of the method has been tested in several cases of steady and unsteady two-dimensional compressible flow. The main focus of the evaluation is on the efficiency and the accuracy of the semi-implicit methods for transient flow simulations when a large CFL number is used to reduce the computational time. The results of all of the test cases show that by using the semi-implicit method the computational efficiency can be improved nearly by one order of magnitude while the high accuracy of the explicit method is maintained. Meanwhile, the CFL numbers in the semi-implicit computations are limited only by streamwise grid sizes and the accuracy requirement for unsteady flow computations. The results have demonstrated the advantage in efficiency by using the high-order semi-implicit time-stepping methods in the DNS of unsteady compressible flows.

Appendix: Jacobian Matrices and Coefficient Matrices

The detailed Jacobian matrices for the viscous flux vector in Eq. (35) for semi-implicit schemes are

$$V = \begin{bmatrix} \rho \\ u \\ v \\ T \end{bmatrix}$$

$$\frac{\partial V}{\partial U} = \begin{bmatrix} 1 & 0 & 0 & 0 \\ \dfrac{u}{\rho} & \dfrac{1}{\rho} & 0 & 0 \\ \dfrac{v}{\rho} & 0 & \dfrac{1}{\rho} & 0 \\ \dfrac{\alpha - e_i}{\rho C_v} & -\dfrac{u}{\rho C_v} & -\dfrac{v}{\rho C_v} & \dfrac{1}{\rho C_v} \end{bmatrix}$$

$$\boldsymbol{A}_v = \frac{1}{J}\begin{bmatrix} 0 & 0 & 0 & 0 \\ 0 & \mu a_{22} & \mu a_{23} & 0 \\ 0 & \mu a_{23} & \mu a_{33} & 0 \\ 0 & a_{42} & a_{43} & k a_{44} \end{bmatrix}$$

$$\boldsymbol{B}_v = \frac{1}{J}\begin{bmatrix} 0 & 0 & 0 & 0 \\ 0 & \dfrac{\partial \mu}{\partial \eta} a_{22} & \dfrac{\partial \mu}{\partial \eta} a_{23} & b_{24} \\ 0 & \dfrac{\partial \mu}{\partial \eta} a_{23} & \dfrac{\partial \mu}{\partial \eta} a_{33} & b_{34} \\ 0 & b_{42} & b_{43} & b_{44} \end{bmatrix}$$

$$\boldsymbol{C}_v = \frac{1}{J}\begin{bmatrix} 0 & 0 & 0 & 0 \\ 0 & 0 & 0 & c_{24} \\ 0 & 0 & 0 & c_{34} \\ 0 & c_{42} & c_{43} & c_{44} \end{bmatrix}$$

where

$$\alpha = \tfrac{1}{2}(u^2 + v^2), \qquad e_i = C_v T$$

where the coefficients in the matrices of $\boldsymbol{A}_v$, $\boldsymbol{B}_v$, and $\boldsymbol{C}_v$ are

$$a_{22} = \frac{4}{3}\eta_x \eta_x + \eta_y \eta_y, \qquad a_{23} = -\frac{2}{3}\eta_y \eta_x + \eta_x \eta_y$$

$$a_{33} = \eta_x \eta_x + \frac{4}{3}\eta_y \eta_y, \qquad a_{42} = \mu(a_{22}u + a_{23}v)$$

$$a_{43} = \mu(a_{23}u + a_{33}v), \qquad a_{44} = \eta_x^2 + \eta_y^2$$

$$b_{24} = a_{22}\frac{\partial u}{\partial \eta}\frac{\partial \mu}{\partial T} + a_{23}\frac{\partial v}{\partial \eta}\frac{\partial \mu}{\partial T}, \qquad b_{34} = a_{23}\frac{\partial u}{\partial \eta}\frac{\partial \mu}{\partial T} + a_{33}\frac{\partial v}{\partial \eta}\frac{\partial \mu}{\partial T}$$

$$b_{42} = a_{22}\left(2\mu\frac{\partial u}{\partial \eta} + u\frac{\partial \mu}{\partial \eta}\right) + a_{23}\left(2\mu\frac{\partial v}{\partial \eta} + v\frac{\partial \mu}{\partial \eta}\right)$$

$$b_{43} = a_{23}\left(2\mu\frac{\partial u}{\partial \eta} + u\frac{\partial \mu}{\partial \eta}\right) + a_{33}\left(2\mu\frac{\partial v}{\partial \eta} + v\frac{\partial \mu}{\partial \eta}\right)$$

$$b_{44} = u\frac{\partial \mu}{\partial T}\left(a_{22}\frac{\partial u}{\partial \eta} + a_{23}\frac{\partial v}{\partial \eta}\right) + v\frac{\partial \mu}{\partial T}\left(a_{23}\frac{\partial u}{\partial \eta} + a_{33}\frac{\partial v}{\partial \eta}\right) + 2a_{44}\frac{\partial k}{\partial \eta}$$

$$c_{24} = a_{22}\frac{\partial^2 u}{\partial \eta^2}\frac{\partial \mu}{\partial T} + a_{23}\frac{\partial^2 v}{\partial \eta^2}\frac{\partial \mu}{\partial T}$$

$$c_{34} = a_{23}\frac{\partial^2 u}{\partial \eta^2}\frac{\partial \mu}{\partial T} + a_{33}\frac{\partial^2 v}{\partial \eta^2}\frac{\partial \mu}{\partial T}$$

$$c_{42} = a_{22}\frac{\partial}{\partial \eta}\left(\mu\frac{\partial u}{\partial \eta}\right) + a_{23}\frac{\partial}{\partial \eta}\left(\mu\frac{\partial v}{\partial \eta}\right)$$

$$c_{43} = a_{23}\frac{\partial}{\partial \eta}\left(\mu\frac{\partial u}{\partial \eta}\right) + a_{33}\frac{\partial}{\partial \eta}\left(\mu\frac{\partial v}{\partial \eta}\right)$$

$$c_{44} = a_{22}\frac{\partial \mu}{\partial T}\frac{\partial}{\partial \eta}\left(u\frac{\partial u}{\partial \eta}\right) + a_{33}\frac{\partial \mu}{\partial T}\frac{\partial}{\partial \eta}\left(v\frac{\partial u}{\partial \eta}\right) + a_{23}\frac{\partial \mu}{\partial T}\frac{\partial}{\partial \eta}\left(v\frac{\partial u}{\partial \eta} + u\frac{\partial v}{\partial \eta}\right) + a_{44}\frac{\partial^2 T}{\partial \eta^2}\frac{\partial k}{\partial T}$$

The detailed coefficient matrices in Eq. (36) are

$$\boldsymbol{A}_{ij} = a_1^1\left(\frac{\partial F_+'}{\partial U}\right)_{ij-3} + a_1^2\left(\frac{\partial F_-'}{\partial U}\right)_{ij-3} - b_1^3 A_v\left(\frac{\partial V}{\partial U}\right)_{ij-3} - a_1^3 B_v\left(\frac{\partial V}{\partial U}\right)_{ij-3}$$

$$\boldsymbol{B}_{ij} = a_2^1\left(\frac{\partial F_+'}{\partial U}\right)_{ij-2} + a_2^2\left(\frac{\partial F_-'}{\partial U}\right)_{ij-2} - b_2^3 A_v\left(\frac{\partial V}{\partial U}\right)_{ij-2} - a_2^3 B_v\left(\frac{\partial V}{\partial U}\right)_{ij-2}$$

$$\boldsymbol{C}_{ij} = a_3^1\left(\frac{\partial F_+'}{\partial U}\right)_{ij-1} + a_3^2\left(\frac{\partial F_-'}{\partial U}\right)_{ij-1} - b_3^3 A_v\left(\frac{\partial V}{\partial U}\right)_{ij-1} - a_3^3 B_v\left(\frac{\partial V}{\partial U}\right)_{ij-1}$$

$$\boldsymbol{D}_{ij} = a_4^1\left(\frac{\partial F_+'}{\partial U}\right)_{ij} + a_4^2\left(\frac{\partial F_-'}{\partial U}\right)_{ij} - b_4^3 A_v\left(\frac{\partial V}{\partial U}\right)_{ij} - a_4^3 B_v\left(\frac{\partial V}{\partial U}\right)_{ij} - C_v\left(\frac{\partial V}{\partial U}\right)_{ij}$$

$$\boldsymbol{E}_{ij} = a_5^1\left(\frac{\partial F_+'}{\partial U}\right)_{ij+1} + a_5^2\left(\frac{\partial F_-'}{\partial U}\right)_{ij+1} - b_5^3 A_v\left(\frac{\partial V}{\partial U}\right)_{ij+1} - a_5^3 B_v\left(\frac{\partial V}{\partial U}\right)_{ij+1}$$

$$\boldsymbol{F}_{ij} = a_6^1\left(\frac{\partial F_+'}{\partial U}\right)_{ij+2} + a_6^2\left(\frac{\partial F_-'}{\partial U}\right)_{ij+2} - b_6^3 A_v\left(\frac{\partial V}{\partial U}\right)_{ij+2} - a_6^3 B_v\left(\frac{\partial V}{\partial U}\right)_{ij+2}$$

$$\boldsymbol{G}_{ij} = a_7^1\left(\frac{\partial F_+'}{\partial U}\right)_{ij+3} + a_7^2\left(\frac{\partial F_-'}{\partial U}\right)_{ij+3} - b_7^3 A_v\left(\frac{\partial V}{\partial U}\right)_{ij+3} - a_7^3 B_v\left(\frac{\partial V}{\partial U}\right)_{ij+3}$$

where a_l^1, a_l^2, b_l^3, and a_l^3 $(l = 1, \ldots, 7)$ are the coefficients of high-order finite difference schemes given by Eqs. (28) and (29). The superscripts 1, 2, and 3 represent the coefficients for the upwind, downwind, and central scheme, respectively.

Acknowledgments

This research was supported by the U.S. Air Force Office of Scientific Research under Grants F49620-95-1-0405 and F49620-97-1-0030 and by the California Space Institute at the University of California under Grant CS-26-97.

References

[1]Kleiser, L., and Zang, T. A., "Numerical Simulation of Transition in Wall-Bounded Shear Flows," *Annual Review of Fluid Mechanics*, Vol. 23, 1991, pp. 495–535.

[2]Erlebacher, G., and Hussaini, M. Y., "Numerical Experiments in Supersonic Boundary-Layer Stability," *Physics of Fluids: A*, Vol. 2, No. 1, 1990, pp. 94–104.

[3]Fasel, H., Thumm, A., and Bestek, H., "Direct Numerical Simulation of Transition in Supersonic Boundary Layer: Oblique Breakdown," *Transitional and Turbulent Compressible Flows*, FED-Vol. 151, American Society of Mechanical Engineers, New York, 1993, pp. 77–92.

[4]Eibler, W., and Bestek, H., "Spatial Numerical Simulations of Linear and Weakly Nonlinear Instabilities in Supersonic Boundary Layers," *Theoretical and Computational Fluid Dynamics*, Vol. 8, No. 3, 1996, pp. 219–235.

[5]Adams, N. A., "Subharmonic Transition to Turbulence in a Flat-Plate Boundary Layer at Mach Number 4.5," *Journal of Fluid Mechanics*, Vol. 317, 1996, pp. 301–335.

[6]Guo, Y., Kleiser, L., and Adams, N. A., "A Comparision Study of an Improved Temporal DNS and Spatial DNS of Compressible Boundary Layer Transition," AIAA Paper 94-2371, June 1994.

[7]Zhong, X., "Additive Semi-Implicit Runge–Kutta Schemes for Computing High-Speed Nonequilibrium Reactive Flows," *Journal of Computational Physics*, Vol. 128, No. 1, 1996, pp. 19–31.

[8]Zhong, X., "High-Order Finite-Difference Schemes for Numerical Simulation of Hypersonic Boundary Layer Transition," *Journal of Computational Physics*, Vol. 144, No. 2, 1998, pp. 662–709.

[9]Yoh, J. J., and Zhong, X., "Low-Storage Semi-Implicit Runge–Kutta Methods for Reactive Flow Computations," AIAA Paper 98-0130, Jan. 1998.

[10]Orszag, S. A., Israeli, M., and Deville, M. O., "Boundary Conditions for Incompressible Flows," *Journal of Scientific Computing*, Vol. 1, No. 1, 1986, pp. 75–111.

[11]Streett, C. L., and Macaraeg, M. G., "Spectral Multi-Domain for Large-Scale Fluid Dynamic Simulations," *Applied Numerical Mathematics*, Vol. 6, No. 1, 1989/90, pp. 123–139.

[12]Poinsot, T. J., and Lele, S. K., "Boundary Conditions for Direct Simulations of Compressible Viscous Flows," *Journal of Computational Physics*, Vol. 101, No. 2, 1992, pp. 104–129.

[13]Collis, S. S., and Lele, S. K., "A Computational Approach to Swept Leading-Edge Receptivity," AIAA Paper 96-0180, Jan. 1996.

[14]Hu, S., and Zhong, X., "Linear Stability of Viscous Supersonic Plane Couette Flow," *Physics of Fluids*, Vol. 10, No. 3, 1998, pp. 709–729.

J. Kallinderis
Associate Editor